

**Elastic and electron-capture processes in  $H^+ + C_2H_4$  collisions below the 10-keV regime**

Reiko Suzuki

*Computer Center, Hitotsubashi University, Kunitachi, Tokyo 186-8601, Japan*

Sachchida N. Rai

*Computer Centre, Bijní Complex, North-Eastern Hill University, Shillong-793003, Meghalaya, India*

Heinz-Peter Liebermann and Robert J. Buenker

*Fachbereich C-Mathematik und Naturwissenschaften, Bergische Universität Wuppertal, D-42119 Wuppertal, Germany*

Lukáš Pichl

*Foundation of Computer Science Laboratory, University of Aizu, Aizu-Wakamatsu, Fukushima 965-8580, Japan*

Mineo Kimura

*Graduate School of Sciences, Kyushu University, Fukuoka 812-8581, Japan*

(Received 15 September 2004; published 14 March 2005)

Electron capture and direct elastic scattering in collisions of  $H^+$  ions with  $C_2H_4$  molecules are studied by using a molecular representation within a semiclassical as well as a fully quantum-mechanical approaches below 10 keV. Calculations are carried out at three different molecular configurations, in which  $H^+$  approaches (i) parallel and (ii) perpendicular to the  $C=C$  axis in the molecular plane, and (iii) perpendicular to this plane. We find that electron capture in the (iii) configuration takes place preferentially over that in the (i) and (ii) configurations at scattering angles above  $15^\circ$ , while the results for (i) and (ii) are comparable in magnitude below  $10^\circ$ , although (ii) dominates slightly at still smaller angles. Total capture cross sections for the (iii) and (ii) configurations differ by a factor of 4 above 500 eV, while those for (i) lie between these values. Below 500 eV, the results for (i) and (iii) are similar in magnitude, while that for the (ii) configuration sharply decreases.

DOI: 10.1103/PhysRevA.71.032710

PACS number(s): 34.70.+e, 34.50.-s, 82.30.Fi

**I. INTRODUCTION**

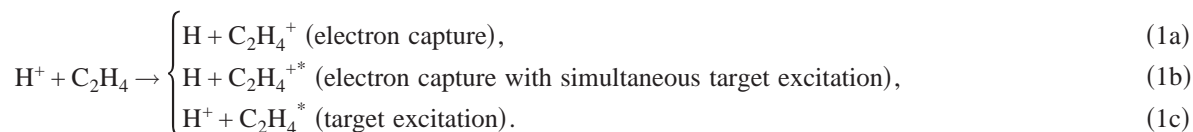
Electron capture in collisions of ions with atoms in the low-keV-energy regions has remained one of the most lively research areas in atomic physics in the last two decades because it provides information fundamental for atomic and molecular spectroscopy and many-body collision dynamics. The study of electron capture is also important for many applications such as nanotechnology, fusion, and medical sciences as well as basic sciences such as atmospheric and astrophysical research. Relatively comprehensive studies involving a variety of atomic targets for a wide range of collision energies (meV to keV), and for various charged projectiles have greatly improved our understanding of electronic structure and dynamics of ions and atoms [1,2]. An increasing volume of cross-section data for electron capture is now becoming available for application.

Unlike the situation for atomic targets, both experimental and theoretical studies of molecular targets are scarce because of inherent complexities in treating molecular targets in both theory and experimental analysis. Even for a relatively active research area like chemical-reaction dynamics, the target species and collision energies are quite limited in rigorous investigations. However, because of recent rapid developments in research areas based on plasma processing and ion-beam technology, a proper theoretical understanding of dynamical aspects as well as the determination of accurate reaction cross sections is urgently required, which in turn

should also help determine optimal running conditions in these technological areas.

Except for the relative wealth of data for  $H_2$ , no similar level of theoretical study has been reported for other molecular targets in the low-to-intermediate-energy regime. Because of this lack of investigation, we have initiated a series of rigorous theoretical studies of elastic and electron-capture processes in the collisions of  $H^+$  ions with various molecules, primarily hydrocarbons, in the region below a few keV down to a few tens of eV. Hydrocarbon molecules are found to exist abundantly in various astrophysical and atmospheric environments, fusion reactors, and plasma-chemistry atmospheres, and are known to play a crucial role in determining a number of physical effects [3]. In this research, we have studied collisions of  $H^+$  ions with  $CH_4$  [4],  $C_2H_2$  [5],  $C_mH_n$  [6], and  $CO$  [7] as well as  $H_2$  and  $D_2$  [8], and this work has shed much light on the isotopic, isomeric, steric, and temperature effects. These findings have had a significant impact on various applications and have also stimulated careful reassessments of previous experimental studies.

In the present work in this series, a more complex system, the ethylene molecule ( $C_2H_4$ ), has been considered in order to study its scattering dynamics for electron capture and excitation and to examine its fragmentation products based on analysis of its dissociation reactions [9]. The processes studied are, in addition to elastic scattering,



We are concerned primarily with electron capture and direct elastic scattering in collisions of  $\text{H}^+$  ions with  $\text{C}_2\text{H}_4$  molecules for energies below 2 keV in order to provide accurate cross-section values. Contribution from the process (1b), i.e., electron capture with simultaneous target excitation, is also examined. The products of process (1c) lie about 4 eV above the initial channel. There are several intermediate charge-transfer channels, and therefore the contribution from the process (1c) is expected to be of negligible relevance in the present energy region. As described above, various kinds of hydrocarbons are produced at the edge-plasma region in fusion reactors such as in divertors. Thus the knowledge of these hydrocarbons and their fragmented species is crucial for accurate determination of carbon chemistry in fusion research. At the same time, we have also examined the fragmentation processes for each of the electronic states calculated.

We obtain our results by using a molecular orbital expansion method within a fully quantum-mechanical as well as a semiclassical formalism. For detailed examination of the collision dynamics, three molecular configurations are specifically considered for direct study: a proton approaches (i) parallel to or (ii) perpendicular to the  $\text{C}=\text{C}$  axis in the molecular plane, and (iii) perpendicular to this plane.

Interferences of various origin are a key subject of fundamental interest in physics, and they also form an essential basis for possible use of this technique for material and surface analysis. Hence, these effects will be emphasized in the present investigation.

## II. THEORETICAL MODEL

The theoretical methods employed are rather standard and have been described more extensively elsewhere [4–7,9].

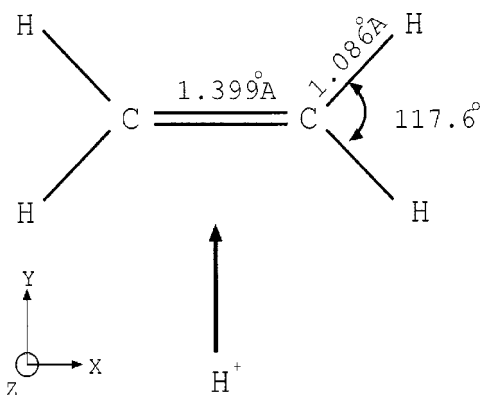


FIG. 1. Schematic diagram indicating the molecular axis orientation employed for the  $[\text{H}+\text{C}_2\text{H}_4]^+$  collision system.

Hence, only a summary of specific features will be given in the present work.

### A. Molecular states

Details of the present molecular calculations, that is, adiabatic potentials, coupling matrix elements, and wave functions, have already been published elsewhere [9]. In brief, the adiabatic potential-energy curves and corresponding wave functions are calculated by means of the multireference single- and double-excitation configuration-interaction (MRD CI) method [10–16], with configuration selection and energy extrapolation. The Table CI algorithm [12,13] is employed for efficient handling of Hamiltonian matrix elements for the many-electron basis functions (symmetrized linear combinations of Slater determinants).

The atomic orbital (AO) basis set in the present calculations consists of contracted Cartesian Gaussian functions. For the carbon atoms a primitive basis ( $10s, 5p, 2d, 1f$ ) contracted to  $[4s, 3p, 2d, 1f]$  due to Dunning [17] is employed. From the same reference, a primitive basis ( $5s, 2p, 1d$ ) contracted to  $[3s, 2p, 1d]$  is used for the hydrogen atoms. AOs with two  $s$  ( $\alpha_s=0.023a_0^{-2}$  and  $0.0055a_0^{-2}$ ), two  $p$  ( $\alpha_p=0.021a_0^{-2}$  and  $0.0049a_0^{-2}$ ), and one  $d$  ( $\alpha_d=0.015a_0^{-2}$ ) exponents have been placed at the midpoint of the  $\text{C}=\text{C}$  bond. The calculations are carried out in the  $C_{2v}$  point group, depending on the approach of the proton toward the midpoint of the ethylene molecule along the three principal axes.

The coordinate system for the projectile and the target molecule of the  $[\text{H}+\text{C}_2\text{H}_4]^+$  collision system is shown in Fig. 1. Table I contains the designations of the various electronic states of the colliding system. The target molecular structure is assumed to be frozen at the equilibrium configuration of the neutral ground geometry [18] during collisions. This restriction is justified since the present collision time is much shorter, less than  $10^{-17}$  s, than the relaxation time of  $10^{-13}$  s, or longer. Hence, only the internuclear distance  $R$  between the  $\text{H}^+$  projectile and the midpoint of the  $\text{C}=\text{C}$  bond was varied in the molecular-state calculations. The  $\text{C}=\text{C}$  bond is placed along the  $x$  axis with its midpoint at

TABLE I. Electronic state designation for three molecular configurations.

Channel	State	(i) config.	(ii) config.	(iii) config.
$\text{H}+\text{C}_2\text{H}_4^+$	X	B1	B1	A1
$\text{H}+\text{C}_2\text{H}_4^{+*}$	A	B2	B2	A2
$\text{H}^++\text{C}_2\text{H}_4$	B	A1	A1	A1
$\text{H}+\text{C}_2\text{H}_4^{+*}$	C	A1	A1	A1

the origin of the coordinate system, and the C—H bonds all lie in the  $xy$  plane, as shown in Fig. 1. The incident projectile approaches the target from three different directions: (i) the proton moves on the  $x$  axis toward the C atom between the H—C—H bonds, (ii) the proton approaches the midpoint of the C=C bond on the  $y$  axis, and (iii) the proton moves along the  $z$  axis toward the midpoint of the C=C.

### B. Collision dynamics

Both fully quantum-mechanical and semiclassical approaches within a molecular representation have been employed, the so-called molecular-orbital close-coupling method. Accordingly, dynamical transitions are driven by nonadiabatic couplings [19].

The total wave function for scattering in a quantum-mechanical approach is described as a product of the electronic and nuclear wave functions, while it is described as a product of a time-dependent coefficient with the electronic wave function in the semiclassical picture. Substitution of the total scattering wave function in a quantum-mechanical approach into the stationary Schrödinger equation yields coupled, second-order differential equations for the nuclear wave functions  $X^a(R)$ . It is computationally convenient to solve the coupled equations in a diabatic representation [19]. The transformation from the adiabatic to the diabatic representation can be readily achieved through a unitary transformation matrix  $C(R)$ . In this representation the nuclear wave function for the heavy particles is given by  $X^d(R) = C^{-1}X^a(R)$ , and the corresponding diabatic potential matrix is defined as  $V^d = C^{-1}V^aC$ , where  $V^a$  is the adiabatic potential matrix. The resulting coupled equations for  $X^d(R)$  are given in matrix form as

$$\left( \frac{1}{2\mu} \Delta_R I - V^d(R) + EI \right) X^d(R) = 0 \quad (2)$$

where  $\mu$  is the reduced mass of the colliding pair and  $I$  is the identity matrix. The coupled equations (2) are solved numerically to obtain the scattering  $S_\ell$  matrix for each partial wave  $\ell$ . The differential cross section as a function of scattering angle  $\theta$  is then obtained from the standard formula by using the scattering  $S_\ell$ -matrix element for partial wave  $\ell$  and the momentum of the projectile. Integration over all angles gives the total scattering cross section.

In the semiclassical approach substitution of the total wave function into the time-dependent Schrödinger equation gives a set of first-order coupled differential equations for the time-dependent coefficients. By solving it numerically, one can obtain the transition amplitudes. Integration of the square product of the amplitude over the impact parameter gives the desired cross sections.

In the present calculations we have carried out up to four-state close-coupling treatments. The corresponding molecular states arise from the initial  $[H^+ + C_2H_4]$ , the electron-capture  $[H + C_2H_4^+]$ , the target excitation  $[H^+ + C_2H_4^*]$ , and the charge transfer with excitation  $[H + C_2H_4^{+*}]$  channels.

## III. RESULTS

### A. Adiabatic potentials and couplings

Extensive results have already been discussed in detail in Ref. [9], and therefore, only specific points relevant to the collision dynamics discussed below are highlighted in the present work.

The adiabatic potentials for the present collision systems for three different configurations (i)–(iii), respectively, are shown in Figs. 2(a)–2(c) and corresponding representative radial and angular coupling matrix elements are depicted in Figs. 3(a) and 3(b), respectively. The initial  $[H^+ + C_2H_4]$  state is the third from the bottom, while the ground  $[H + C_2H_4^+]$  state after charge transfer is the lowest and the second and the fourth correspond to electronically excited  $[H + C_2H_4^{+*}]$  states. The valence electron in the first two states possesses  $\pi$  character, while the higher two are  $\sigma$  in nature for the (i) and (ii) configurations. Hence, the angular coupling is expected to be the primary cause of the transition from the initial state to charge-transfer channels. For the (iii) configuration, all states have  $\sigma$  character, and hence radial couplings among them are the primary cause of the dynamics.

As specific characteristics of the potential curves, for the (i) and (ii) configurations, the initial state, the third from the lowest, crosses the first and second states because of the different symmetry, while the initial and fourth states show rather parallel nature for all  $R$ . Therefore, for (i) and (ii), transitions due to the angular coupling mechanism are expected to be more efficient than those allowed by radial coupling at the lower-energy side. For the (iii) configuration, except for the ground-state potential, all curves are repulsive, hence increasing with decreasing  $R$ , and they do not show any hint of strong avoided crossings among them because the interactions are due to relatively weak polarization potentials. This suggests that a Demkov-type mechanism for charge transfer is expected to play an important role. Hence, depending on the proton path taken, very different collision dynamics can be anticipated, i.e., there is a strong steric effect. This feature will be considered in more detail below. Representative radial and angular coupling matrix elements which connect the initial and dominant charge-transfer channels are shown in Figs. 3(a) and 3(b).

### B. Differential cross sections

Differential cross sections (DCSs) for the (i)-, (ii)-, and (iii)-configurations at 0.5 keV (left panel) and 1.5 keV (right panel), respectively, are shown in Figs. 4(a)–4(c) over the entire range of scattering angle. DCS angles up to  $10^\circ$  are also depicted separately in Figs. 5(a)–5(c) for the three configurations. Figure 6 shows the DCSs averaged over the three molecular configurations.

Direct elastic scattering processes are found to dominate in magnitude over electron capture for all cases at all energies and for most scattering angles. Beyond the scattering angle of  $10^\circ$  all DCSs show very weak angle independency up to roughly  $150^\circ$ . Then, for all cases at 1.5 keV, electron-capture DCSs for backward scattering beyond  $150^\circ$  jump by two to three orders of magnitude, indicating that electron

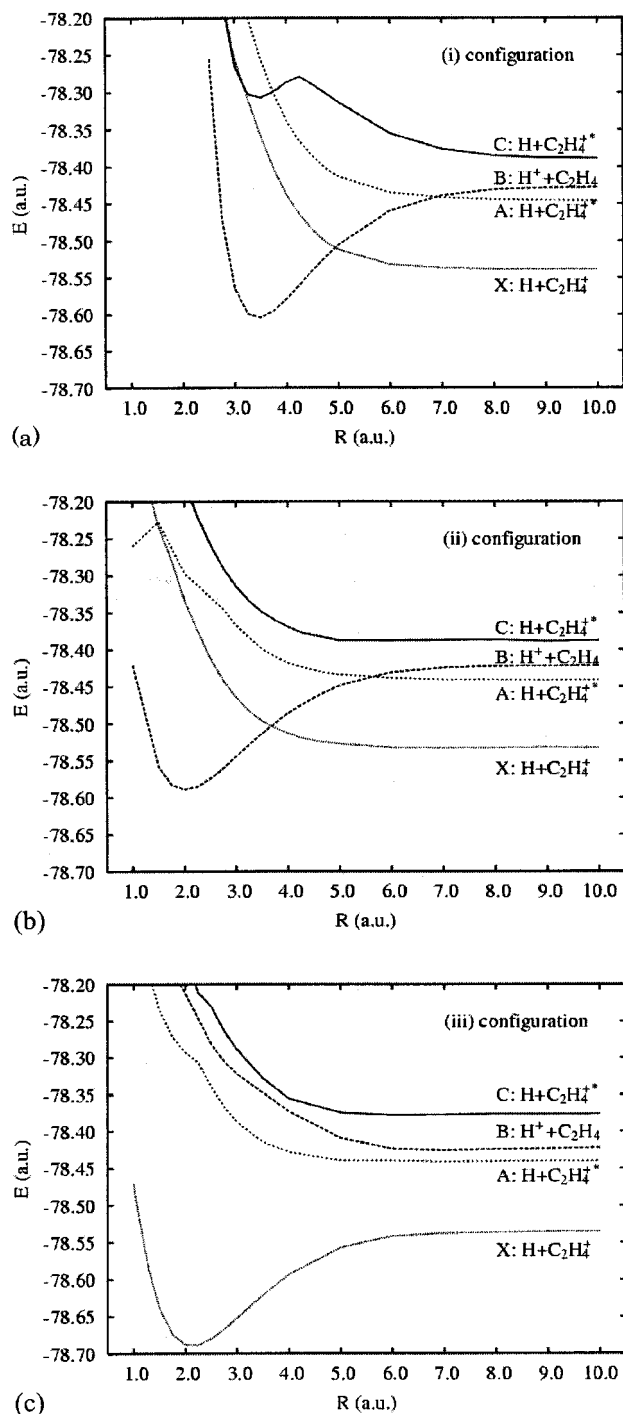


FIG. 2. The adiabatic potentials of the  $[H+C_2H_4]^+$  system for the (a) (i), (b) (ii), and (c) (iii) directions of approach of the proton.

capture suddenly becomes efficient. This feature becomes more marked as the energy increases from 0.5 to 1.5 keV, as can be seen from Fig. 6, suggesting that efficient electron capture and strong recoil occur simultaneously.

Although most of the complex irregular oscillatory patterns seen for all cases are due to interferences between elastic and electron-capture channels, there are clues for some structures which suggest that multiple scatterings inside the molecule also play a role in these cases. When the projectile

enters the molecular field, it is rather strongly influenced by the different atomic centers in the molecule, i.e., there is multiple scattering. This feature is also manifested in the peaks in radial couplings. In order to examine this effect more clearly, we include  $s$ -matrix elements as a function of angular momentum  $\ell$  for three configurations at 0.5 keV in Fig. 7. In addition to small but high-pitched oscillations, large gradual irregular oscillatory structures can be seen in all  $s$ -matrix elements, and these are most likely due to the multiple-scattering effect (see also the coupling in Fig. 3), particularly those for  $\ell$  larger than 1000. These oscillatory features are quite different in pattern from those for atomic and symmetrical molecular cases where oscillatory patterns generally show more regular structures. Further, the present oscillatory features differ significantly depending on the molecular configuration, which is a manifestation of the steric effect. These oscillatory structures indicate that the electron jumps back and forth between the projectile and target continuously during a single collision, i.e., electron capture and electron loss. At the exit, the favored process becomes either direct elastic scattering or electron capture; hence there is interference between these two possibilities as a function of the collision energy and the impact parameter.

Since all three configurations exhibit similar magnitudes for the DCSs as well as similar overall shape, the general features seen in the averaged DCSs (Fig. 6) are easily deduced from these three DCSs. This can be clearly noticed when DCSs in the region of  $10^\circ$  to  $60^\circ$  are examined. The sharp dip at around  $28^\circ$  in the (i) configuration and several small dips in the (ii) configuration disappear, becoming a single broad peak similar to the DCSs in the (iii) configuration.

### C. Partial cross sections

Partial cross sections are illustrated in Figs. 8(a)–8(c) for formation of the ground as well as excited  $C_2H_4^+$  ions after charge transfer for the three configurations. For the (i) configuration, the  $C$ -state population is far dominant in all energies over the other two, while the  $A$ -state population is second largest. The  $X$ - and  $A$ -state populations synchronize with each other, suggesting a strong coupling between the two states. For the (ii) configuration, the  $C$ -state population becomes dominant above 1.5 keV, while the  $A$ -state population is important below this energy. The  $X$ -state population is the weakest in most of the energy range except for the region below 0.3 keV, where it overtakes the  $C$  population. For the (iii) configuration, the  $X$ -state population is dominant above roughly 0.5 keV, followed by that of the  $A$ -state, while below this energy that of the  $C$  state dominates, with the  $A$  state next. The differences observed above are a manifestation of a strong steric effect.

The averaged values for the three configurations are shown in Fig. 9. The order of the present computed magnitudes of each cross section for most of the energy region is configuration (ii) > (iii) > (i). For the (ii) configuration, the projectile passes through the molecular area of the highest charge concentration, while the (i) configuration corresponds to the least interaction with the molecule, and hence this

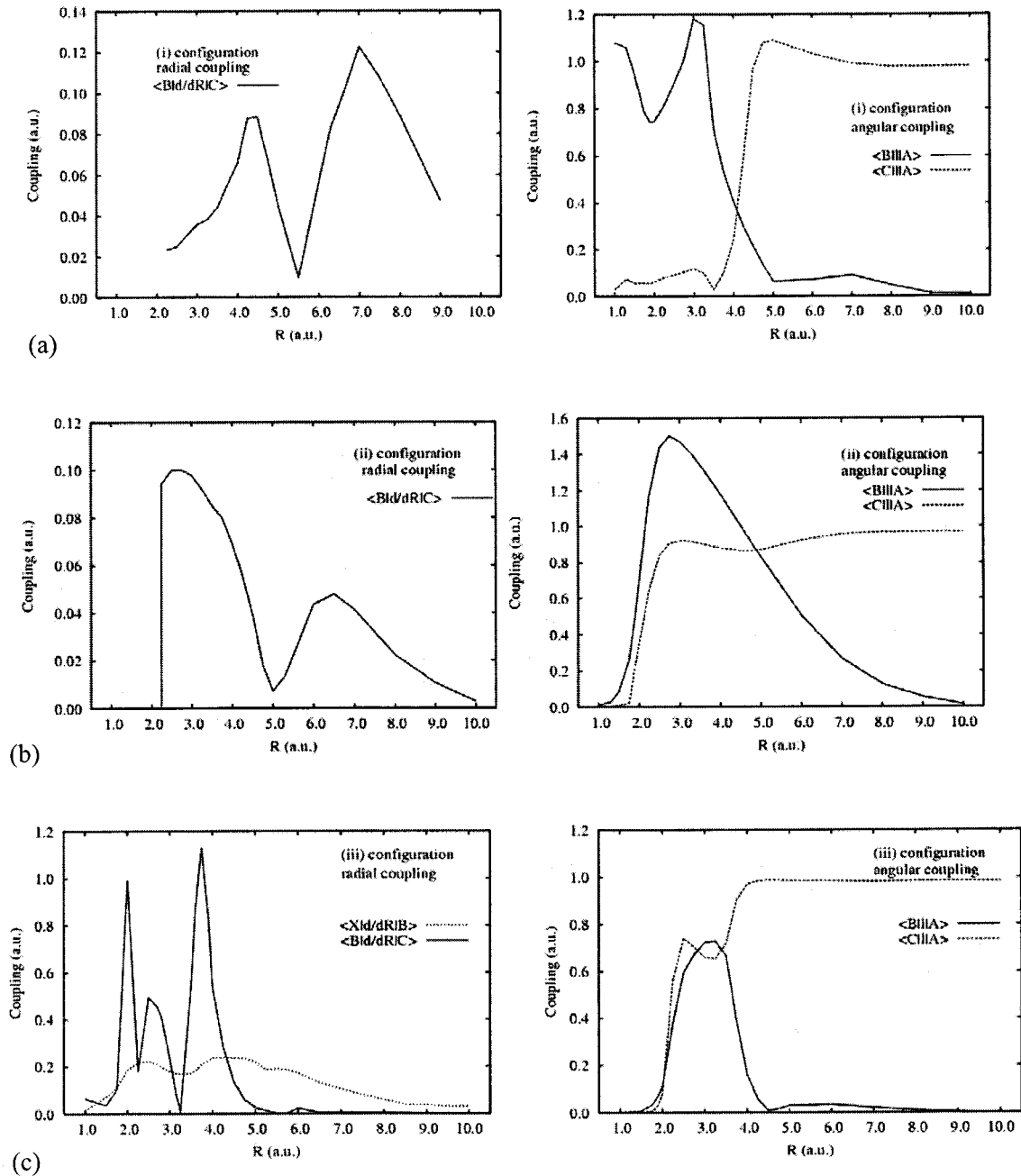


FIG. 3. Representative radial (left panel) and angular (right panel) couplings between the initial and electron-capture states for the (a) (i), (b) (ii), and (c) (iii) configurations.

order for the cross sections seems reasonable. When transition probabilities as a function of collision time at a fixed impact parameter and energy were carefully investigated (not shown), more oscillatory structures in the probability were observed in the (i) configuration because the interaction time is longer compared to that in the (ii) and (iii) configurations. This feature increases the probability of electron transfer back to the target, that is, an electron loss from the projectile, in the (i) configuration, thus reducing the cross section.

#### D. Total cross sections

The sum of all electron-capture cross sections for the three configurations is shown in Fig. 10 along with those

averaged over the configurations from 0.1 to 10 keV. As is apparent, the results for the (i) and (iii) configurations have large cross sections with a value of  $(1-2) \times 10^{-15} \text{ cm}^2$  and a rather weak energy dependence, while that for the (ii) configuration shows a sharp increase from a value of  $1.6 \times 10^{-16} \text{ cm}^2$  at 150 eV to  $7 \times 10^{-16} \text{ cm}^2$  at 600 eV. This feature may be simply understood from the fact that for the (i) configuration, the molecular size is larger by nearly a factor of 2 than it is for the (ii) configuration, and hence the interaction time is longer. This has a large influence on the size of the cross section.

There have been two early experimental attempts to measure charge transfer at relatively high energy above 100 keV

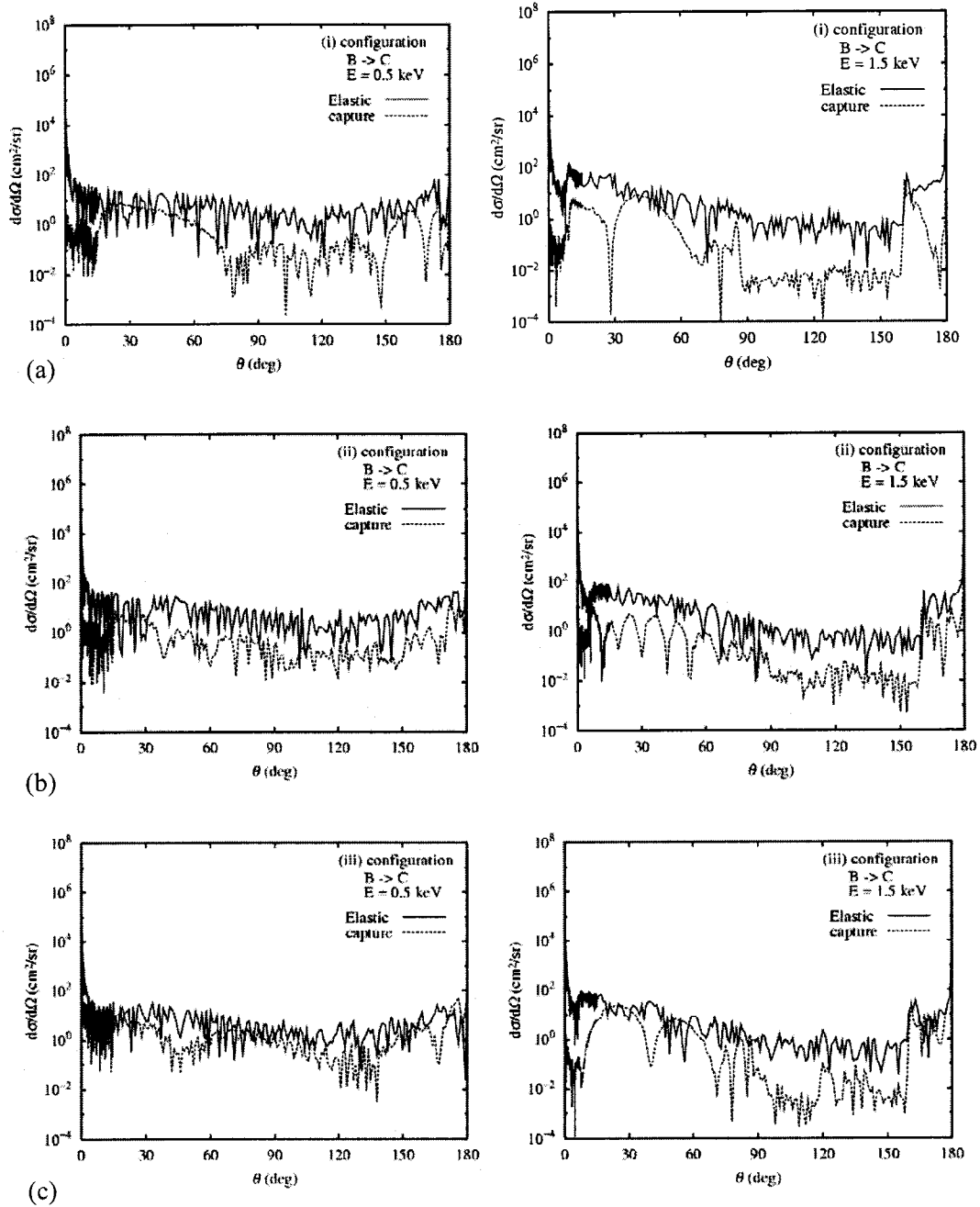


FIG. 4. Differential cross sections for the (a) (i), (b) (ii), and (c) (iii) configurations at 0.5 (left panel) and 1.5 keV (right panel) from the initial state  $B$  to the electron-captured state  $C$ . Solid line, direct elastic scattering; dashed line, electron capture.

by Toburen *et al.* [20], and above 1.0 MeV by Varghese *et al.* [21]. The measured results by Toburen *et al.* give a value of approximately  $1.5 \times 10^{-16} \text{ cm}^2$  at 100 keV, decreasing to  $2.5 \times 10^{-18} \text{ cm}^2$  at 280 keV. The other set of measurements by Varghese *et al.* gives a value of  $5.1 \times 10^{-21} \text{ cm}^2$  at 2 MeV. There is one more recent measurement of electron capture by Sanders *et al.* [22] in the energy range from 60 to 120 keV. At 60 keV, their value is reported to be  $3.57 \times 10^{-16} \text{ cm}^2$ , but it decreases to  $0.625 \times 10^{-16} \text{ cm}^2$  at 120 keV, which is smaller by a factor of 2 compared to the earlier measurement of Toburen *et al.* discussed above. The present results, although for much lower energy, appear to connect smoothly with the high-energy measurements upon extrapolation.

Janev *et al.* [23] derived an analytical formula for fitting charge-transfer cross sections of  $\text{H}^+ + \text{C}_n\text{H}_m$  collisions based on the Demkov approximation by evaluating a large set of experimental data. This formula has also been employed for interpolation and extrapolation of experimental data by them and they claim that their analytical formula is able to estimate experimental results within an order of magnitude at 10 keV/u. For the lower-energy side from 0.1 to 1 keV/u, they provide the result by simply fitting the data of by Toburen *et al.* [20], although the usage of the results by Toburen *et al.* may need some care.

Figure 11 includes our total charge-transfer cross sections of the present system along with those estimates by Janev *et al.*

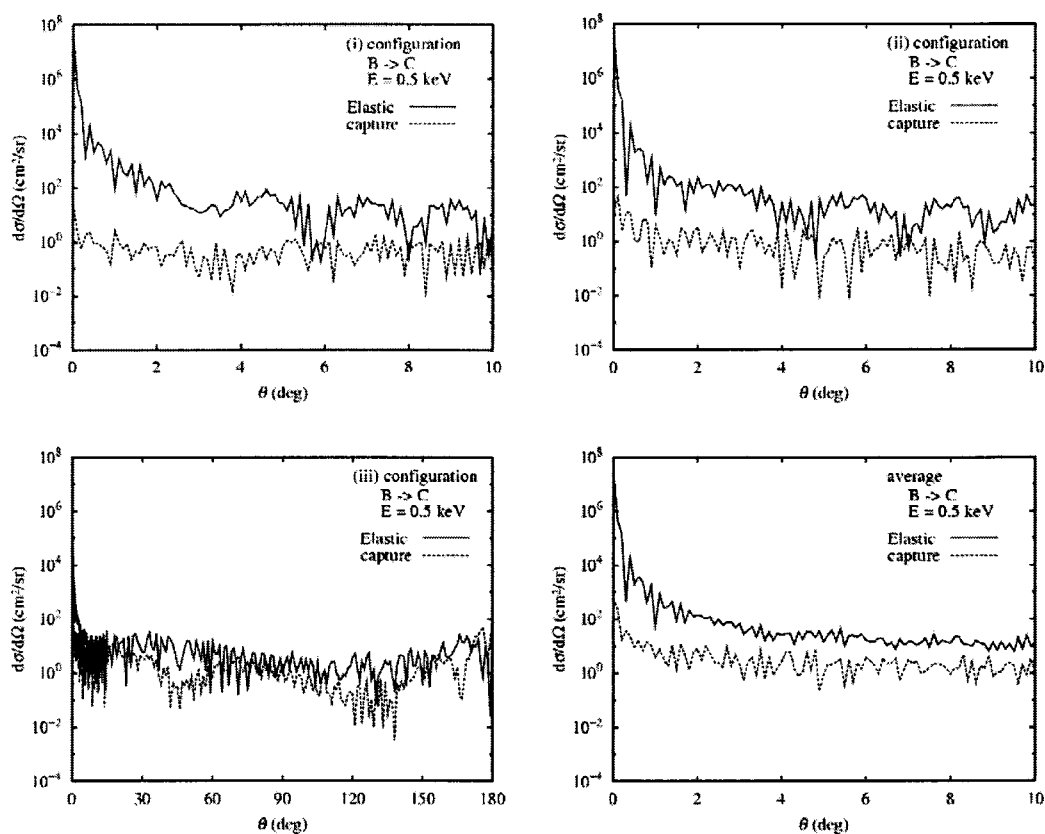


FIG. 5. Differential cross sections for small scattering angles up to  $10^\circ$  at 0.5 keV from the initial state  $B$  to the electron-capture state  $C$  are shown. Solid line, direct elastic scattering; dashed line, electron capture.

*al.* Generally, both results give a similar magnitude of the cross section within a value of  $(1-3) \times 10^{-15}$  cm<sup>2</sup>, but show slightly different energy dependence. Janev *et al.*'s results are found to be larger by a factor of 2 than our result in the lower-energy region below 0.3 keV. Their result shows a gradual decrease in the higher-energy region, while ours increases monotonically. Finally these two sets of data merge at a collision energy of 10 keV. Since, as discussed, the analytical formula by Janev *et al.* is based on a somewhat crude approximation and although this formula provides a useful guideline for the fitting, a high-accuracy result is not expected to be reproduced by this formula.

### E. Comparison of capture cross sections with CH<sub>4</sub>, C<sub>2</sub>H<sub>2</sub>, C<sub>2</sub>H<sub>6</sub>, and C<sub>3</sub>H<sub>8</sub>

In order for us to examine the possible relationship between the magnitude of the electron-capture cross section and molecular quantities such as the number of total atoms in hydrocarbons, or the number of valence electrons in a molecule, we have plotted the cross sections as a function of the number of atoms in the molecule in Fig. 12, including our previous electron-capture cross-section data for CH<sub>4</sub>, C<sub>2</sub>H<sub>2</sub>, C<sub>2</sub>H<sub>6</sub>, and C<sub>3</sub>H<sub>8</sub> below 10 keV. At the lower-energy side, the order of the cross sections is clearly apparent as C<sub>3</sub>H<sub>8</sub> > C<sub>2</sub>H<sub>6</sub> > CH<sub>4</sub> > C<sub>2</sub>H<sub>4</sub> > C<sub>2</sub>H<sub>2</sub>. This is suggestive that the

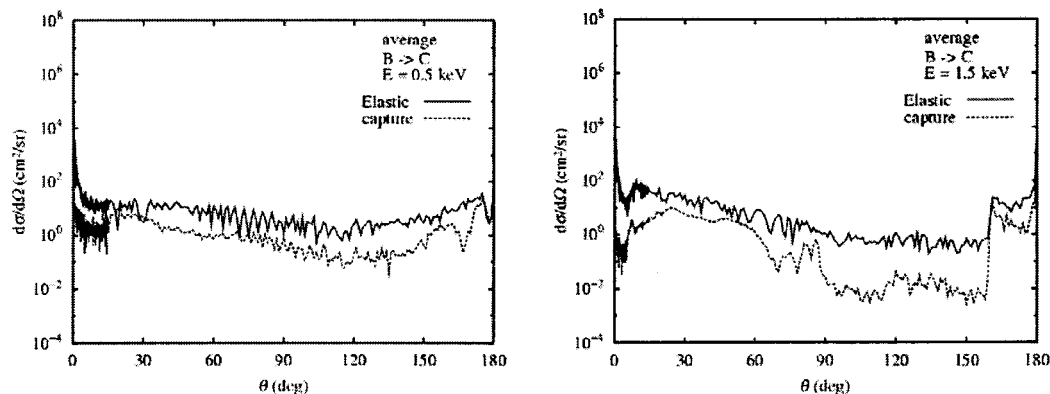
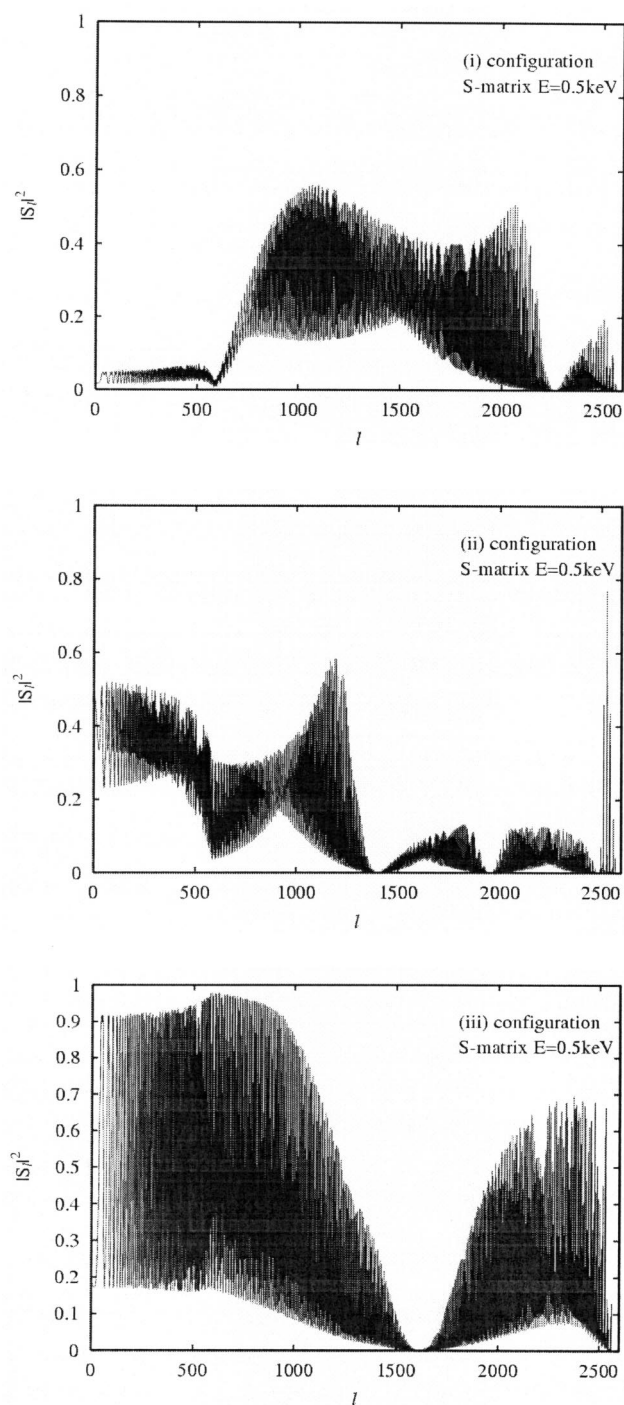


FIG. 6. Differential cross sections averaged over three configurations.

FIG. 7. *S*-matrix elements for three configurations.

magnitude of the cross section depends on the number of atoms in a molecule, except for the case of  $\text{CH}_4$ , since its cross section is higher than that of both  $\text{C}_2\text{H}_4$  and  $\text{C}_2\text{H}_2$  and thus is somewhat irregular in this respect. The origin of this feature may arise from the nature of the bonding:  $\text{C}_2\text{H}_2$ ,  $\text{C}_2\text{H}_4$ , and  $\text{C}_2\text{H}_6$  have a triple, double, and single bond, respectively, and for these hydrocarbons the major portion of the charge distribution depends on the nature of this C—C bonding. Therefore, as the binding order increases, the more the electron distribution is concentrated in the C—C bond

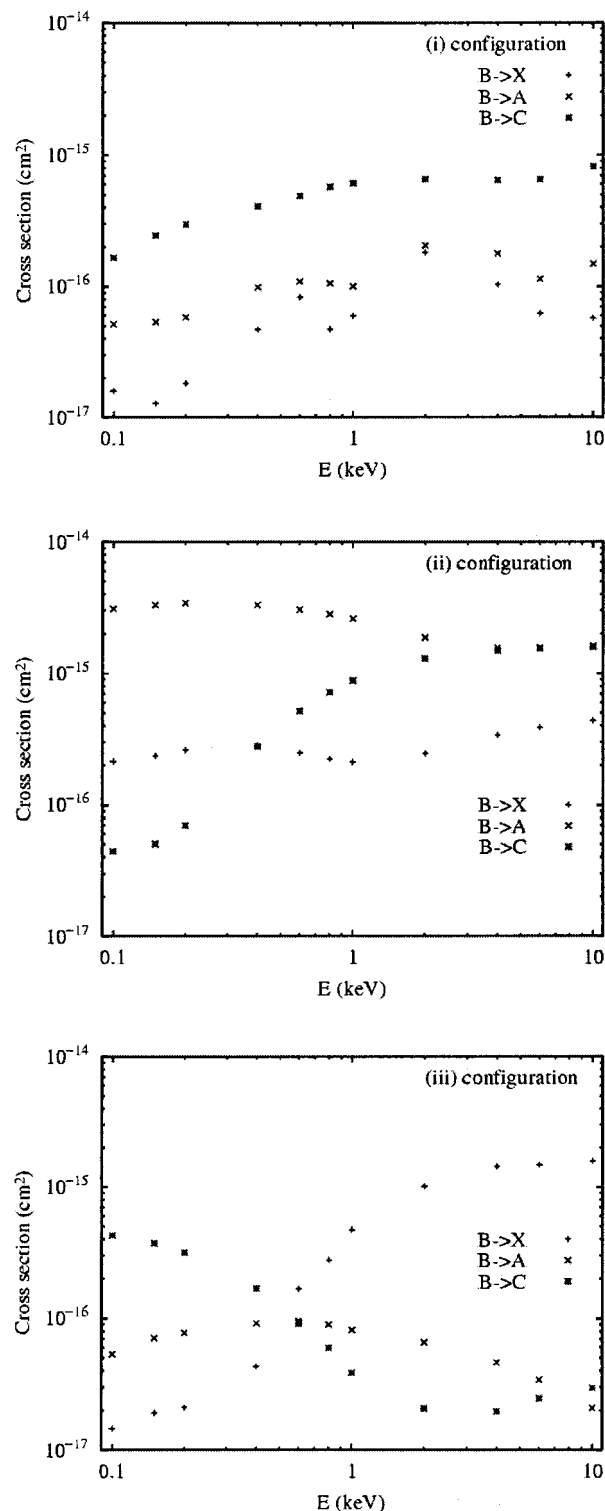


FIG. 8. Partial cross sections from each channel for the (i), (ii), and (iii) molecular configurations.

and becomes localized within a narrow spatial region, thus causing a smaller geometrical size and hence reducing the effective scattering region, as reflected in the sizes of the cross section for these three hydrocarbons. Since  $\text{CH}_4$  has only four single bonds, and its charge distribution is somewhat more broadly spread out compared to its counterparts

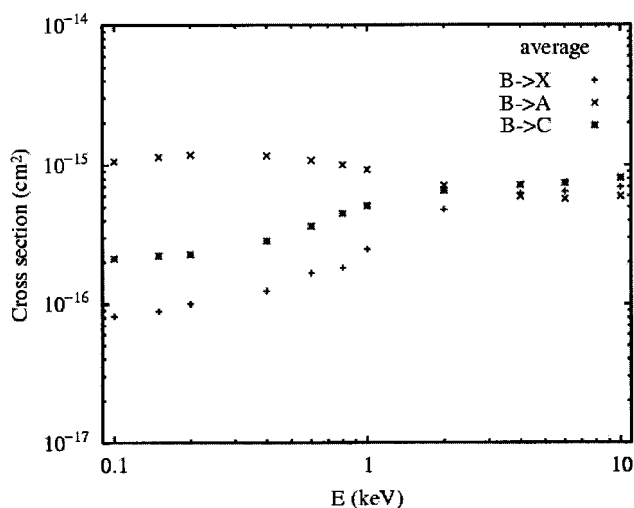


FIG. 9. The averaged partial cross sections for the X-, A-, and C-state populations.

with double and triple bonds, thus increasing the effective size of the molecule. The C—H bond lengths for  $\text{CH}_4$ ,  $\text{C}_2\text{H}_2$ ,  $\text{C}_2\text{H}_4$ , and  $\text{C}_2\text{H}_6$  are 1.094, 1.058, 1.086, and 1.094 Å, respectively. Indeed, the cross section for  $\text{CH}_4$  is only slightly smaller in magnitude than that of  $\text{C}_2\text{H}_6$  where  $\text{C}_2\text{H}_6$  has a cigarlike shape, but only single bonds are present and hence it is more similar in charge distribution with  $\text{CH}_4$ . The ionization potentials are known to be 12.51, 11.4, 10.5, and 11.52 eV, respectively [24]. Therefore, the magnitude of ionization potential does not appear to correlate closely with that of the cross-section size, at least in this range of collision energy. Note that the ionization potential for  $\text{CH}_4$  is the highest among them.

At higher energy above 3 keV or so, the differences in size of the cross section of the various molecules become much narrower because of the increasingly shorter interaction time, making it less sensitive to the individual physical characteristics of each molecule. From around this energy

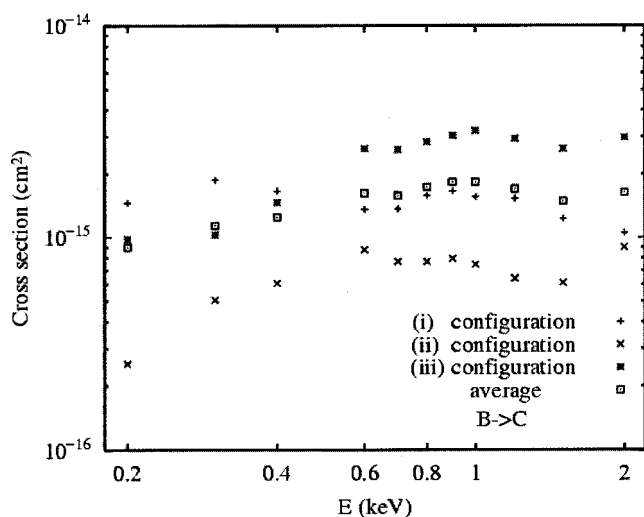


FIG. 10. Electron-capture total cross sections.

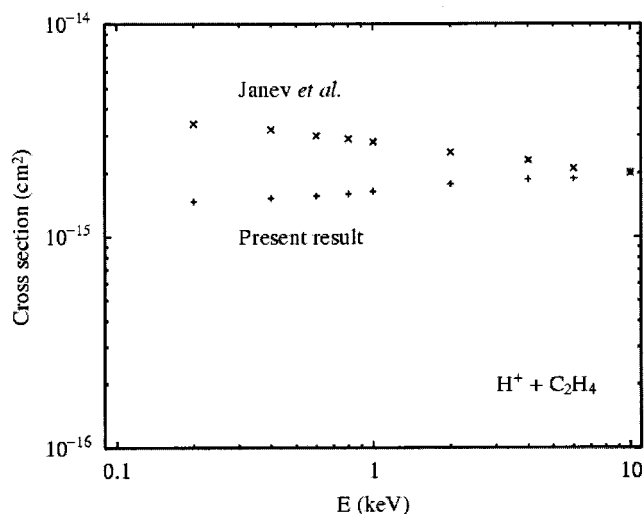


FIG. 11. Total electron-capture cross sections of the  $\text{H}^+ + \text{C}_2\text{H}_4$  system along with the estimates by Janev *et al.* [23].

and above, the incoming projectile may be viewed as interacting with the individual atoms in a molecule rather than with the molecule as a whole, and this is the basis for the additivity rule discussed in Ref. [22]. As a result, the present energy region investigated is not consistent with the additivity rule, and it is doubtful that it holds at all, at least in this energy domain.

### F. Fragmentations

The calculations described above are carried out under the assumption that the ethylene molecule will not decompose as a result of collisions with  $\text{H}^+$  ions, i.e., the frozen-target approximation. Based on the energy levels obtained, it is nonetheless possible to provide some insight regarding dissociation fragments, as discussed below. There are a number of other possibilities [25], however, which need to be taken into account when considering the results of the present cross-

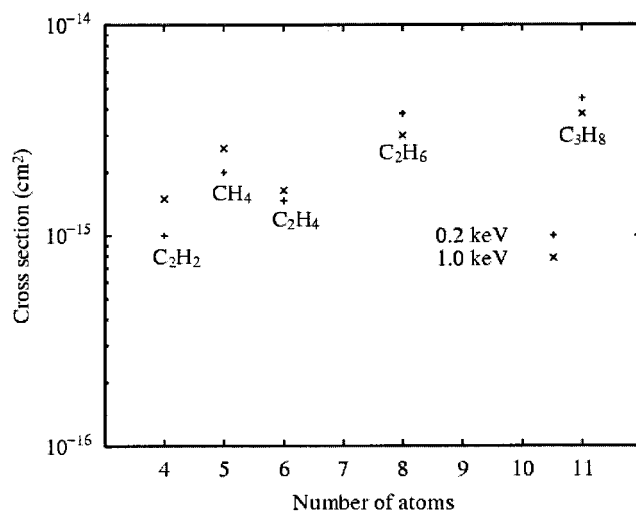


FIG. 12. Total cross sections as a function of the number of atoms in the molecule.

section calculations. The dissociation energy of ethylene itself is 7.55 eV when the C=C bond is broken, leading to a pair of CH<sub>2</sub> (methylene) molecules in their ground (<sup>3</sup>B<sub>1</sub>) state. The latter can further dissociate to produce carbon atoms, H<sub>2</sub>, and H<sub>3</sub><sup>+</sup>. Breaking a single bond of methylene requires an additional 4.2 eV for products of CH (<sup>2</sup>Π)+H. The corresponding bond energy for CH is 3.47 eV. The dissociation energy of one C—H bond in ethylene is slightly higher, 4.8 eV, typically leading to products of a C<sub>2</sub>H<sub>3</sub> radical plus H<sub>2</sub>, whereby 2.24 eV (0.5 times the dissociation energy of H<sub>2</sub>) is retrieved from the recombination of H atoms.

If a pair of C—H bonds is broken, the most likely products are acetylene (C<sub>2</sub>H<sub>2</sub>) and H<sub>3</sub><sup>+</sup>. Dissociation of three C—H bonds can produce the C<sub>2</sub>H molecule plus H<sub>3</sub><sup>+</sup> and H, or C<sub>2</sub>H plus two H<sub>2</sub> molecules. Finally, if all four C—H bonds are broken, the products are C<sub>2</sub>, H<sub>3</sub><sup>+</sup>, and H<sub>2</sub> or C<sub>2</sub> and two H<sub>2</sub> molecules. The dissociation energy of the double bond of the C<sub>2</sub>H<sub>3</sub> radical is 7.16 eV, while that of the triple bond of acetylene is 10.0 eV. Depending on the excess en-

ergy available during the H<sup>+</sup> collisions, it is therefore seen that a large number of ethylene fragmentations can occur.

#### ACKNOWLEDGMENTS

This work was supported in part by a Grant-in-Aid from the Ministry of Education, Science, Sport, Culture and Technology, the Japan-Germany Collaborative Research Program of the Japan Society for Promotion of Science, a Cooperative Research Grant from the National Institute for Fusion Science, Japan (R.S., L.P., and M.K.), and a JSPS Grant-in-Aid for young scientists (L.P.). The financial support of the Fonds der Chemischen Industrie and the Deutsche Forschungsgemeinschaft (Grant No. Bu:450/7-3) is gratefully acknowledged (R.J.B., H.P.L., and S.N.R.). One of us (S.N.R.) thanks the North-Eastern Hill University, Shillong, India, for granting a study leave to him at the University of Wuppertal during the course of the present work.

- 
- [1] E. W. McDaniel, J. B. A. Mitchell, and M. E. Rudd, *Atomic Collisions* (Wiley Interscience, New York, 1993).
- [2] B. H. Bransden and C. J. Joachain, *Ion-Atom Collisions* (Oxford University Press, New York, 1993).
- [3] H. Tawara, Y. Itikawa, H. Nishimura, H. Tanaka, and Y. Nakamura, *At. Plasma-Mater. Interact. Data Fusion* **2**, 41 (1992).
- [4] M. Kimura, Y. Li, G. Hirsch, and R. J. Buenker, *Phys. Rev. A* **52**, 1196 (1995).
- [5] M. Kimura, Y. Li, G. Hirsch, and R. J. Buenker, *Phys. Rev. A* **54**, 5019 (1996).
- [6] T. Kusakabe, K. Asahina, A. Iida, Y. Tanaka, Y. Li, G. Hirsch, R. J. Buenker, M. Kimura, H. Tawara, and Y. Nakai, *Phys. Rev. A* **62**, 062715 (2000).
- [7] T. Kusakabe, K. Asahina, J. P. Gu, G. Hirsch, R. J. Buenker, M. Kimura, H. Tawara, and Y. Nakai, *Phys. Rev. A* **62**, 062714 (2000).
- [8] T. Kusakabe, M. Kimura, L. Pichl, R. J. Buenker, and H. Tawara, *Phys. Rev. A* **68**, 050701(R) (2003).
- [9] Note that a part of the molecular-structure calculations was published by us earlier. See S. N. Rai, H.-P. Liebermann, R. J. Buenker, and M. Kimura, *Int. J. Quantum Chem.* **95**, 866 (2003).
- [10] R. J. Buenker and S. D. Peyerimhoff, *Theor. Chim. Acta* **35**, 33 (1974).
- [11] R. J. Buenker and S. D. Peyerimhoff, *Theor. Chim. Acta* **39**, 217 (1975).
- [12] S. Krebs and R. J. Buenker, *J. Chem. Phys.* **103**, 5613 (1995).
- [13] R. J. Buenker, in *Proceedings of the Workshop on Quantum Chemistry and Molecular Physics, Wollongong, Australia*, edited by P. Burton (University Press, Wollongong, 1980).
- [14] E. R. Davidson, in *The World of Quantum Chemistry*, edited by R. Daudel and B. Pullman (Reidel, Dordrecht, 1974), p. 17.
- [15] R. J. Buenker, D. B. Knowles, S. N. Rai, G. Hirsch, K. Bhannuprakash, and J. R. Alvarez-Collado, in *Studies in Physical and Theoretical Chemistry*, edited by R. Carbo (Elsevier, Amsterdam, 1989), Vol. 62, p. 181.
- [16] D. B. Knowles, J. R. Alvarez-Collado, G. Hirsch, and R. J. Buenker, *J. Chem. Phys.* **92**, 585 (1990).
- [17] T. H. Dunning, Jr., *J. Chem. Phys.* **98**, 1007 (1989).
- [18] G. Herzberg, *Molecular Spectra and Molecular Structure* (Van Nostrand Reinhold, New York, 1966), Vol. III.
- [19] M. Kimura and N. F. Lane, *Adv. At., Mol., Opt. Phys.* **26**, 79 (1990).
- [20] L. H. Toburen, Y. Nakai, and R. A. Langley, *Phys. Rev.* **171**, 114 (1968).
- [21] S. L. Varghese, G. Bissinger, J. M. Joyce, and R. Laubert, *Phys. Rev. A* **31**, 2202 (1985).
- [22] J. M. Sanders, S. L. Varghese, C. H. Fleming, and G. A. Soonai, *J. Phys. B* **36**, 3835 (2003).
- [23] R. K. Janev, J. G. Wang, and T. Kato, NIFS Report No. DATA-64, 2001.
- [24] *CRC Handbook of Chemistry and Physics*, edited by D. R. Lide (CRC Press, Boca Raton, FL, 2000).
- [25] Stephen J. Blanksby and G. Barney Ellison, *Acc. Chem. Res.* **36**, 255 (2003).